Identifying the Farm Fields Irrigated out of Season with GF-1 Satellite Images

Qiaomei Su , Jin Lv , Jinlong Fan * , Weili Zeng , Rong Pan , Yuejiao Liao , Ying Song , Chunliang Zhao , Zhihao Qin , Pierre Defourny

Posted Date: 9 August 2023

doi: 10.20944/preprints202308.0764.v1

Keywords: Irrigation Map; Irrigation fields; Classification; GF-1

Article

Identifying the Farm Fields Irrigated out of Season with GF-1 Satellite Images

Qiaomei Su [1], Jin Lv [2,3], Jinlong Fan [2,*], Weili Zeng [1,2], Rong Pan [1,2], Yuejiao Liao [1,2], Ying Song [1,2], Chunliang Zhao [2,5], Zhihao Qin [4,5], Pierre Defourny [6]

[1] Department of Surveying and Mapping, College of Mining Engineering, Taiyuan University of Technology, Taiyuan, China;
[2] National Satellite Meteorological Center, Beijing, China;
[3] School of Public Administration, China University of Geosciences, Wuhan, China;
[4] College of Geographic Science and Planning, Nanning Normal University, Nanning, China;
[5] MOA Key Laboratory of Agricultural Remote Sensing, Institute of Agro-Resources and Regional Planning, Chinese Academy of Agricultural Sciences, Beijing, China;
[6] Earth and Life Institute, Université Catholique de Louvain, Louvain-la-Neuve, Belgium
* Correspondence: via fanjl@cma.gov.cn

Abstract: Irrigation is one of key agricultural management practices of crop cultivation in the world. Irrigation practice is traceable on satellite image. Most irrigated area mapping methods were developed based on time series of NDVI or back scatter coefficient within the growing season. However, it found the winter irrigation out of growing season is also dominating in north China. This kind of irrigation aims to increase the soil moisture for coping with spring drought, and also reduce the wind erosion with the wet soil in the field surface as the strong wind happens in spring. This study developed a remote sensing-based classification approach to identify irrigated fields with Radom Forest algorithm out of growing season. The results showed that the mean of the highest accuracies of 7 RF models was 94.9% and the mean of the averaged accuracies of 7 RF models was 94.1%; the overall accuracy for all 7 outputs was in the range of 86.8-92.5%, Kappa in the range of 84.0-91.0% and F-1 score in the range of 82.1-90.1%. These results showed that the classification was acceptable and not over performed as the accuracies of all classified images were lower than the models. This study also found that irrigation started to apply in early November and irrigated fields were increased and suspended in December and January due to freeze. The newly irrigated fields were found again in March and April when the temperature goes up above zero degree. The area of irrigated fields in the study area were increasing over time with sizes of 98.6, 166.9, 208.0, 292.8, 538.0, 623.1, 653.8 km^2 from December to April, accounting for 6.1%, 10.4%, 12.9%, 18.2%, 33.4%, 38.7%, and 40.6% of the total irrigatable land in the study area, respectively.

Keywords: irrigation map; irrigation fields; classification; GF-1

1. Introduction

Irrigation is one of key agricultural management practices of crop cultivation in the world [1–4]. Irrigation reduces adverse effect of drought, increases crop yield, and finally maintains a good agricultural production profit. Irrigation consumes a lot of water resources and thus efficient water use management requires timely irrigation information in large region [5]. Irrigated crop land, irrigation event and irrigation water amount are of importance information in support of sustainable water resource management. Studies on hydrology [6], water availability and water use [7], and their interaction with agricultural production and food security [8] all require accurate information on the location and extent of irrigated croplands. The detailed knowledge about the timing and the amounts of water used for irrigation over large areas [3] is also of importance for various studies and applications.

Irrigation practice is traceable on satellite image [9]. A few of global irrigation maps such as the Global Map of Irrigated Areas (GMIAs) [10] and the Global Irrigated Area Map (GIAM) [11] have

 doi:10.20944/preprints202308.0764.v1

become available. Recently, Wu [12] retrieved a 30-m resolution global maximum irrigation extent (GMIE) using the Normalized Difference Vegetation Index (NDVI) and NDVI deviation (NDVIdev) thresholds in the dry and driest months. Zajac [13] derived the European Irrigation Map for the year 2010 (EIM2010) underpinned by the agricultural census data. Siddiqui [14] developed irrigated area map for Asia and Africa regions using canonical correlation analysis and time lagged regression at 250 m resolution for the year 2000 and 2010. Zhang [15] produced annual 500-m irrigated cropland maps across China for 2000–2019, using a two-step strategy that integrated statistics, remote sensing, and existing irrigation products into a hybrid irrigation dataset. Zhao [16] developed crop class based irrigated area maps for India using net sown area and extent of irrigated crops from the census and land use land cover data at 500 m spatial resolution for year 2005. Ambika [17] developed annual irrigated area maps at a spatial resolution of 250 m for the period of 2000-2015 using data from the Moderate Resolution Imaging Spectroradiometer (MODIS) and high-resolution land use land cover (LULC) information in India. Krishnankutty [18] developed high-resolution irrigated area maps for all the agroecological zones in India for the period of 2000-2015, using 250 m MODIS NDVI data and 56 m land use/land cover data. Gumma [19] mapped irrigated agricultural areas for Ghana, using remote sensing methods and protocols with a fusion of 30 m and 250 m spatial resolution remote-sensing data. Xie [20] mapped the extent of irrigated croplands across the conterminous U.S. (CONUS) for each year in the period of 1997–2017 at 30 m resolution, using the generated samples along with remote sensing features and environmental variables to train county-stratified random forest classifiers annually.

Most irrigated area mapping methods above-mentioned were based on time series of NDVI at a relatively low resolution of 250-1000 m. Disaggregating statistics data on the grid is another way to generate the irrigation maps. For example, the European irrigation map (EIM) [21] was created by disaggregating regional-level statistics on irrigated cropland areas into a 100×100m grid, using a land cover map and constrained by the Global Map of Irrigated Areas (GMIAs) [10]. Remote sensing-based classification approach is also a great way to produce the irrigated crop maps. Salmon [22] used supervised classification of remote sensing, climate, and agricultural inventory data to generate a global map of irrigated, rain-fed, and paddy croplands. Lu [23] tried to use pixel-based random forest to map irrigated areas based on 2 scenes of GF-1 satellite images at 16 m in an irrigated district of China, during the winter-spring irrigation period of 2018. Magidi [24] developed a cultivated areas dataset with the Google Earth Engine (GEE) and further used the normalized difference vegetation index (NDVI) to distinguish between irrigated and rainfed areas. A large variety of classification methods at different scales and showing various levels of accuracy can be found in the literature [25–32]. A bunch of applications and the tool of cloud based and open source in classification have been developed recently [33,34]. However, the cloudy contamination and revisit time of optical satellite put a major limitation to accurately identify irrigation signature on the imagery. SAR imagery is less impacted by the cloud, and has advantage on building a long time series data to detect the irrigation signature. Studies [35–37] used timer series of SAR images to detect the irrigation event. The fusion of optical and SAR time series images for classification is also progressing well in recent years [38–40] in order to reduce the cloudy issue on the optical image. Study [41] assessed the value of satellite soil moisture for estimating irrigation timing and water amounts.

All these studies abovementioned were designed to identify the irrigation signature mainly in growing season as crop develops. However, irrigation also happens out of season due to various reasons, like sufficient water supply out of season, cheaper water prices and lower energy prices as well as manpower availability. The kind of irrigation practice aims to keep enough soil moisture for sowing crops at the beginning of growing season in spring in avoid of irrigation water competition and in preparation for coping with spring drought. In this study area, it found a great number of fields already irrigated in winter and in early spring although fields are bare soil and a large volumes of irrigation water were applied to the fields. This kind of irrigation practice should be given more attentions as the winter irrigation is dominating in this region. Therefore, this study aimed to develop a method to identify the irrigated fields and help irrigation authorities know the irrigation situation before the growing season is coming and improve their water supply capacity in the whole year as

 doi:10.20944/preprints202308.0764.v1

such the crop production may be maintained stable. This case also complements the consideration from those researchers who are developing irrigation map within growing season for a large area or at a global level.

2. Study Area and Data

2.1. Study area

The study area locates in the midstream of Fen river in the center of Shanxi province in North China (Figure 1). The study area is also called Jinzhong basin with a size of 150 km length and 30-40 km width and a total area of approximate 5000 km^2. There are three rivers, namely, Fen river, Wenyu river and Xiao river. Irrigation in this basin has a long history of over 1000 years. Fen River irrigation area covers 1046.1 km^2 arable land crossing 3 cities and a million farmers [42]. Wenyu river is a tributary of Fen river and its irrigation area covers 341.8 km^2 arable land [43]. Xiao river irrigation area covers 221.7 km^2 arable land [44]. Irrigation facilities were built in this study area and the flooding irrigation is still dominating trough the irrigating channel to the fields. This study area is one of major grain production areas in Shanxi province and is of importance for regional food security. The main staple crops are maize, sorghum and winter wheat. There are also various orchards trees, greenhouse for vegetable and other crop fields. The growing season is traditionally from May to September. However, winter wheat can grow in this area over the winter time. The winter wheat is planted from the beginning to the later middle of October. After the harvest of winter wheat, only may the short life span crops be planted in avoid of frost in early autumn. At present, a few fields are used to plant winter wheat and most fields are in bare soil in winter. Therefore, the winter irrigation is actually applied to the bare fields. Most fields are cultivated with maize in Summer and maize is in favor of winter irrigation. In term of the climate condition, this study area belongs to the temperate continental seasonal climate zone and a year has 4 seasons, namely, spring, summer, autumn and winter. There is less rainfall in winter and spring while most rainfall happens in summer.

Preprints (www.preprints.org) | NOT PEER-REVIEWED | Posted: 9 August 2023 doi:10.20944/preprints202308.0764.v1

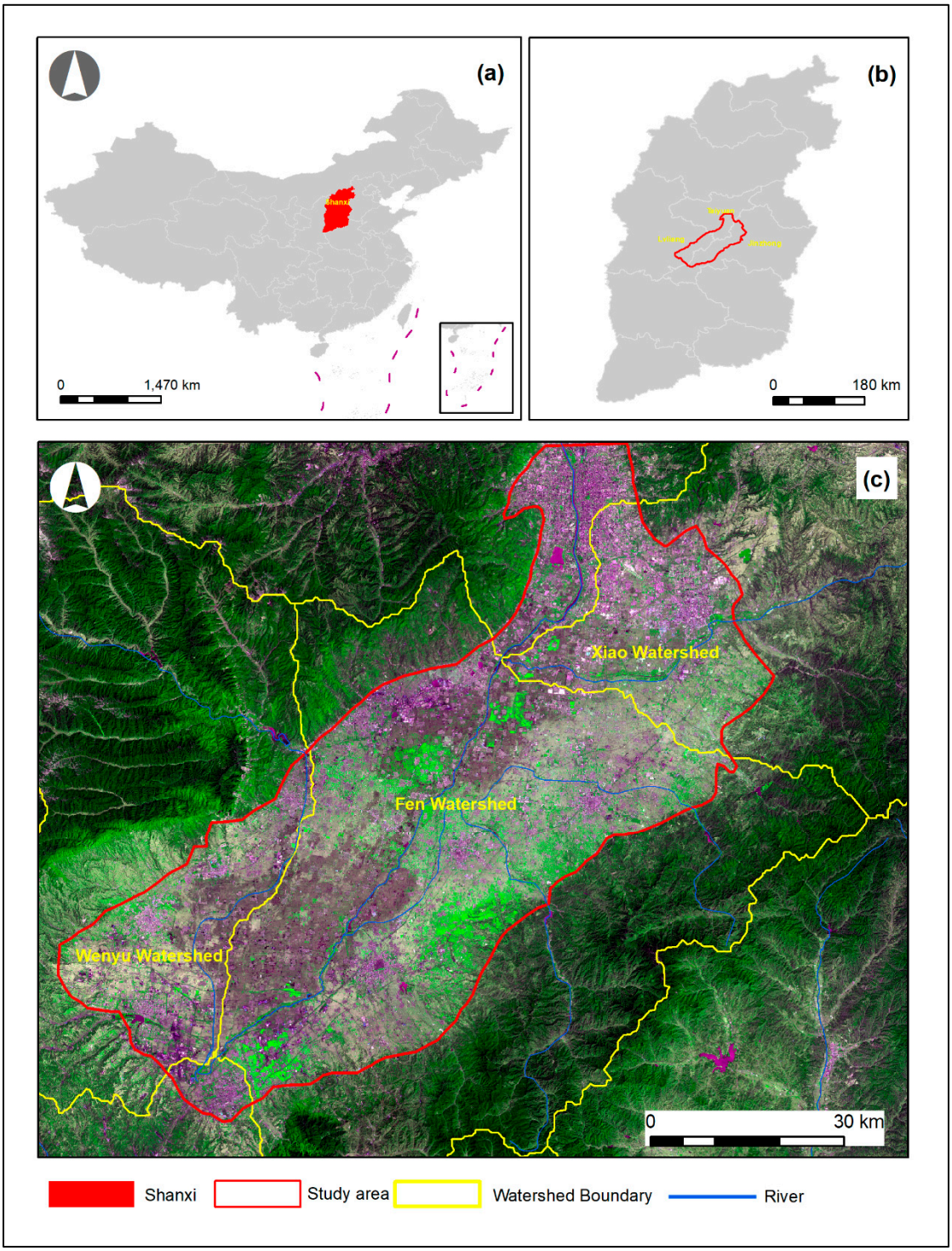

Figure 1. The location of the study area: (a) shows the Shanxi province in China, (b) shows the study area in Shanxi province, and (c) shows the study area illustrated on the GF-1 image on Apr. 29, 2023, respectively.

2.2. Satellite data and processing

GF, the acronym of Gaofen in Chinese and high resolution in English, is one of key Earth observation programs in China. As the first satellite of the Chinese High Resolution Earth Observation System, GF1 Satellite was successfully launched in April 26, 2013 [45]. 4 sets of multiple spectral cameras (wide field of view, WFV) were equipped onboard GF-1 and had a mosaiced swatch of 800 km at 16-meter spatial resolution and a 4-day revisit frequency [46]. As one of limitations in comparison with other high resolution satellite imagery, WFV has only 4 bands listed in the Table 1.

Preprints (www.preprints.org) | NOT PEER-REVIEWED | Posted: 9 August 2023 doi:10.20944/preprints202308.0764.v1

The L1B data of GF-1 WFV data in this study were collected from National Satellite Meteorological Center, China. After the visual check of all images, the images with less than 25% cloud coverage were selected and processed for this study. Thereafter, the FLAASH approach was used to perform the atmospheric correction [47]. Considering that GF-1 had a relatively large geometric errors after the L1B geometrical correction using the RPC Orthorectification approach [47], therefore, a 10m Sentinel-2B image obtained on Oct. 17, 2022 was used as the reference image to co-register all GF-1 images with the image chip matching method. The results for the co-registration of all GF-1 images will be reported in another article in preparation. The images in the same day were mosaiced and tailored to the study area. The finally available images were listed in the Table 2. Due to partial cloud contamination, the satellite data in November and February were removed and the final valid data fit in 7 dates. In order to make a compatible with other high resolution satellite data, the spatial resolution of GF-1 WFV in this study was set to 15 meters, not 16 meters as expected normally.

Table 1. Band Specification and Spatial Resolution of GF-1 WFV.

Band number	Central wavelength(nm)	Bandwidth(nm)	Resolution(m)
1	485	70	16
2	555	70	16
3	660	60	16
4	830	120	16

Table 2. The used GF-1 WFV data.

No.	1	2	3	4	5	6	7
Date	2022/12/27	2023/01/04	2023/01/25	2023/03/03	2023/03/27	2023/0408	2023/0429

2.3. Field data and training samples

A 3-day field campaign was carried out in February 24-26, 2023. During the field campaign, the georeferenced pictures were taken with a GPS camera along the roads following predefined itineraries in the study area. At home, the land cover classes with the longitude and latitude coordinates were retrieved by visually screening pictures with the tool developed for the photo data interpretation [48–50]. During the field campaign, irrigated fields were partially frozen and waterlogged and it was also easy to identify on the satellite images. The final output of this process was a formatted file gathering all GPS points with corresponding classes, class codes, author, roadside (left or right), collecting dates and times and the corresponding picture file names. Finally, 3616 ground truth pictures were valid and with spatial reference. All those sample points were distributed over the study area as shown in the Figure 2.

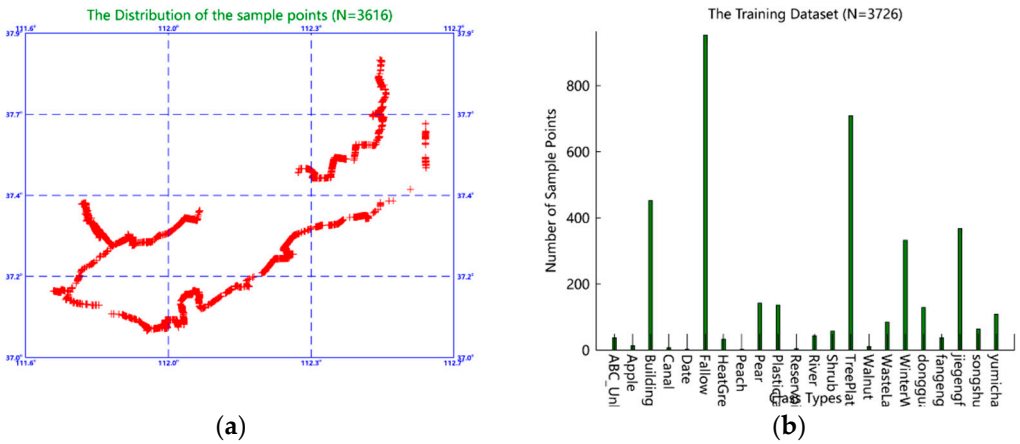

(a) (b)

Figure 2. The distribution(a) and type(b) of field samples in the study area.

Preprints (www.preprints.org) | NOT PEER-REVIEWED | Posted: 9 August 2023 doi:10.20944/preprints202308.0764.v1

The field samples include built-up, water body, tree, orchards, irrigated filed, bare land, winter wheat, green house, and others. These samples are point-based ground truth and not ideally and evenly distributed in the study area. These field samples were used for further collecting more and well distributed training and validation samples by visually interpreting satellite images. The final samples were randomly separated into two groups with a ratio of 70% to 30%. The 70% parts of samples were used to build the classification model and perform the classification and 30% for the validation of classified image. Following our previous experiences [48–50], the distance between two samples was taken into accounts in the sample separation process. In case that both are too close, all pixels in adjacent area were choose as either training or validation. For instance, all samples at the level of image pixel taken in one field represented only one class, so it is good to treat them as one big sample. The threshold of the distance in this study was set as 900 meters. This step avoids the strong spatial correlation among samples. Table 3 lists the description of all classes identified for final classification. Table 4 lists the number of samples and the proportion for each class at 15-meter level for this study. Due to a large volume of water applied to the field and weak evaporation in winter, no classification samples for irrigation 2 were identified on Dec. 17, Jan. 4 and Jan. 25. The irrigation 2 represents the fields with the high soil moisture but without surface water. In the other dates, the two kinds of irrigation conditions in the field were able to be identified.

Table 3. Land cover types and their brief descriptions.

	Class	Acronym	Description
Cropland	Irrigation 1	I1	Waterlogged or Frozen field after irrigation
	Irrigation 2	I2	Field with high soil moisture after irrigation
	Winter Wheat	WW	Winter wheat field
	Straw Covered Cropland	SC	Cropland covered by the straw or other residues out of season
	Bare Cropland	BC	Bare and no covered cropland out of season
	Greenhouse	GH	Greenhouse for vegetable or other cash crops
	Orchards	OC	Fruit trees plantation
	Plantation	PL	Cropland planted with wood or shrub trees
Non Cropland	Built-up	BU	Artificial area including building, road, and factory
	Barren Land	BL	No vegetation covered area in rock mountain
	Deciduous Forest	DF	Deciduous tree and shrub
	Evergreen Forest	EF	Coniferous tree and shrub
	Water Body	WB	Lake, River, Dam, and other Water body

Table 4. The number of training samples and the proportion for each class.

DATE \Class	2022.12.27		2023.01.04		2023.01.25		2023.03.03		2023.03.27		2023.04.08		2023.04.29	
	No.(Pixel Counts)	Proportion(%)	No.(Pixel Counts)	Proportion(%)	No.(Pixel Counts)	Proportion(%)	No.(Pixel Counts)	Proportion(%)	No.(Pixel Counts)	Proportion(%)	No.(Pixel Counts)s	Proportion(%)	No.(Pixel Counts)	Proportion(%)
BC	1898	9.2	1705	7.9	1604	7.8	1466	7.1	1602	8.3	1569	7.8	1485	7.7
BL	1071	5.2	1015	4.7	1045	5.1	1085	5.2	1052	5.5	957	4.8	1014	5.3
BU	7349	35.6	6836	31.8	7662	37.3	7502	36.1	6873	35.6	7403	36.8	7077	36.8
DF	1466	7.1	1214	5.6	1339	6.5	1402	6.7	1319	6.8	1347	6.7	1259	6.5
EF	2067	10	2016	9.4	2067	10.1	2089	10	2139	11.1	1801	8.9	2060	10.7
GH	704	3.4	2561	11.9	695	3.4	745	3.6	687	3.6	514	2.6	700	3.6

Preprints (www.preprints.org) | NOT PEER-REVIEWED | Posted: 9 August 2023 doi:10.20944/preprints202308.0764.v1

I1	1588	7.7	1523	7.1	1562	7.6	879	4.2	812	4.2	459	2.3	371	1.9
I2	0	0	0	0	0	0	1327	6.4	1408	7.3	2587	12.8	1461	7.6
OC	342	1.7	436	2.1	402	2	347	1.7	374	1.9	399	2	531	2.8
PL	121	0.6	204	0.9	108	0.5	167	0.8	158	0.8	112	0.6	118	0.6
SC	1111	5.4	1051	4.9	829	4	770	3.7	391	2	164	0.8	155	0.8
WB	2278	11	2407	11.2	2114	10.3	2412	11.6	1806	9.4	1968	9.7	2140	11.2
WW	622	3.1	546	2.5	623	3	602	2.9	674	3.5	858	4.2	879	4.5
Total	20617	100	21514	100	20544	100	20793	100	19295	100	20138	100	19250	100

3. Methodology

3.1. Classification flowchart

Figure 3 presents the flowchart for this study. The GF-1 WFV satellite data from November, 2022 to April, 2023 was collected and processed. The main processing steps include calibration, geometric and atmospheric correction. The calibration coefficients are available from the web portal [51]. In order to make all GF-1 images geometrically match each other, all images were co-registered with one scene of 10 m Sentinel-2 image obtained on Oct. 17, 2022. Then, all finely co-registered images were mosaiced based on observing date and tailored to the study area. At the same period, the field data were collected and used to support the visual interpretation on each image to prepare the classification samples. The classification samples corresponding to each image were separated into training and validation sets by a ratio 70% to 30%. In next step, a Random Forest classifier was used to execute the classification with each image and corresponding training samples. The classified image was checked by validation samples and expert knowledge visually. The classification samples were further tuned accordingly by increasing or removal of some samples until the result was acceptable. Once the accuracy is acceptable, the final classified map is the output and the final accuracy is reported. Considering the irrigation changes over time, the training samples and validation samples were collected separately based on each image. The classification was carried out one image by one image and not worked with time series [52,53]. When all classified images were done, the final maps and statistics were made for analysis.

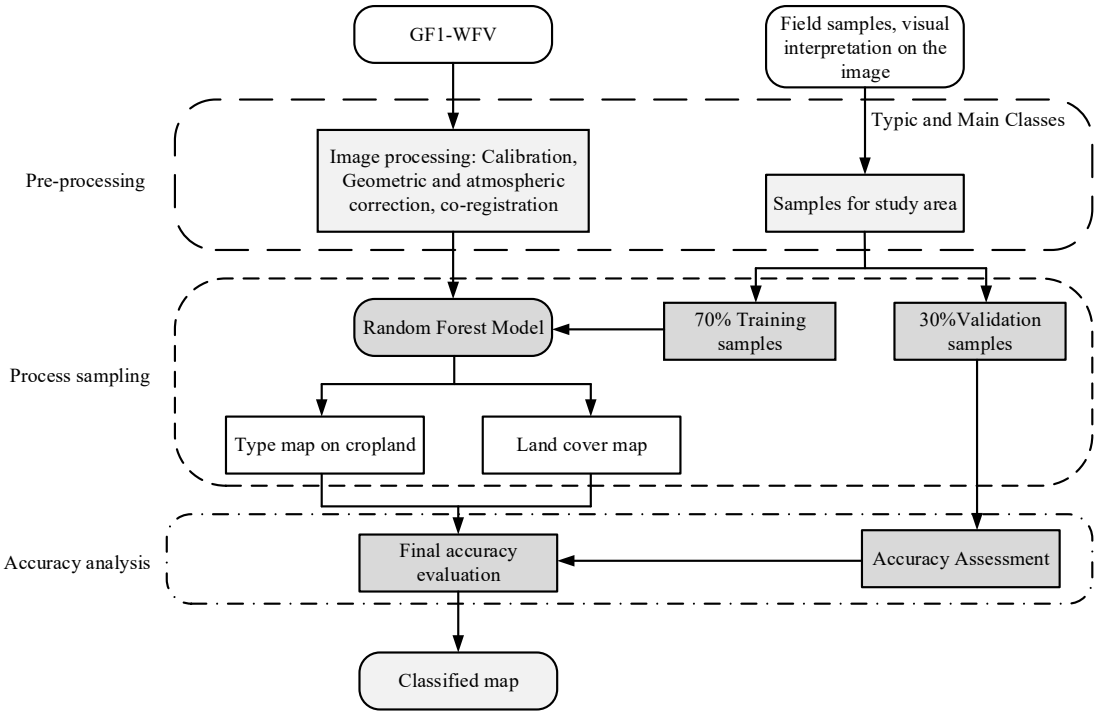

Figure 3. The flowchart for this study.

Preprints (www.preprints.org) | NOT PEER-REVIEWED | Posted: 9 August 2023 doi:10.20944/preprints202308.0764.v1

3.2. Classifier algorithm

The supervised classification algorithm is widely used at present. In supervised classification, the training samples must provide in association with the input images. The final class for each pixel is decided by the classifier. Random Forest (RF) is a supervised machine learning algorithm and a kind of ensemble of the decision tree. RF becomes the popular classifier in recent years as it is robust and easy to apply and only few parameters need to be set and tuned accordingly. Many literatures [34,48,53,54] have proved that the accuracy from RF often overperforms other supervised classifiers, e.g. ML and SVM. The detailed algorithm of RF may refer to the literature [55–59]. RF has only two key parameters to be considered. One is the number of features and another is the number of trees. In this study, the number of features was set as the square root of the number of input bands of the image. After the tests, 100 was set for the number of the tree. More features may increase the accuracy of the classified image. Every two spectral bands may be used to calculate a NDVI like index [50]. So, in this study, all possible NDVI like indices were calculated and added with 4 spectral bands as the input features for the final classification.

3.3. Validation methods

The error confusion matrix [48–50] is usually used to quantitatively evaluate the accuracy of the classified image. The Table 5 lists the typic error confusion matrix. The overall accuracy, OA, the Kappa, and F1-scores may be further calculated based on the error confusion matrix. In the Table 5, the i represents the ground truth and j represents the classified result. The Nij is the number of pixels that were the class i according to the ground truth but were classified to the class j in the resulting image. The J is the digital code of each crop type class.

Table 5. Typical error confusion matrix.

		Classified			
		j = 1	j = 2	...	j = J
Ground Truth	i = 1	N_{11}	N_{12}		N_{1J}
	i = 2	N_{21}	N_{22}		N_{2J}
	...				
	i = J	N_{J1}	N_{J2}		N_{JJ}

The overall accuracy gives the proportion of fully correct classes in the validation samples and can be computed as Equaiton (1), where i, j and Nij donates the same meanings as the abovementioned, respectively.

$$\text{Overall Accuracy OA} = \frac{\sum_{i=1}^{J} N_{ii}}{\sum_{i=j=1}^{J} N_{ij}} \quad (1)$$

Kappa can be computed as Equation (2), where, M donates the total number of validation samples, the others have same meanings as abovementioned. The Kappa coefficient is questionable in evaluation of the accuracy of the classified image. The Kappa coefficient is good to evaluate the unbalanced validation samples but it is difficult to understand the meaning or what Kappa represents. Kappa gives a sense that how much probability of mistake was avoided in the classification process.

$$\text{Kappa} = \frac{M \sum_{i=j=1}^{J} N_{ij} - \sum_{i=j=1}^{J} N_i N_j}{M^2 - \sum_{i=j=1}^{J} N_i N_j} \quad (2)$$

In addition, the F1-Score is also used to evaluate the classified image. The F1-score (Equation (5)) is derived from the precision and the recall for each class, which are computed through Equations (3) and (4) respectively. It gives an indication of the classification performance per

Preprints (www.preprints.org) | NOT PEER-REVIEWED | Posted: 9 August 2023 doi:10.20944/preprints202308.0764.v1

class.

$$\text{Precision}=\frac{N_{ii}}{\sum_{j=1}^{J} N_{ij}} \quad (3)$$

$$\text{Recall}=\frac{N_{jj}}{\sum_{i=1}^{J} N_{ij}} \quad (4)$$

$$\text{F1-score}=2*\frac{\text{Precision}*Recall}{\text{Precision}+Recall} \quad (5)$$

In this study, the validation of each classified images was carried out separately with its independent validation samples. The statistic was computed by counting the number of pixels for each class.

4. Results and analysis

4.1. The Classification Model Accuracy analysis

The accuracy of the classified model determines the top boundary of accuracy that classification may reach reasonably. The higher the model accuracy goes, the higher the classification accuracy may reach. Figure 4 shows the accuracies of out of bag of all models of Random Forest algorithm. The accuracy of out of bag is increasing as the number of trees increases and the accuracy reaches the plateau after 30 tries. In this study, the number of trees was set to 100 and it should be reasonable according to the Figure 4. There were slight differences among all these models but the difference range was quite small and in a range of about 2%. Figure 5 shows the averaged value and maximum value of model accuracy in the range of plateau taken from 50-100 in this study. The averaged highest accuracy for 7 models was 94.9% and the averaged mean accuracy was 94.1%. These data show that all models were acceptable.

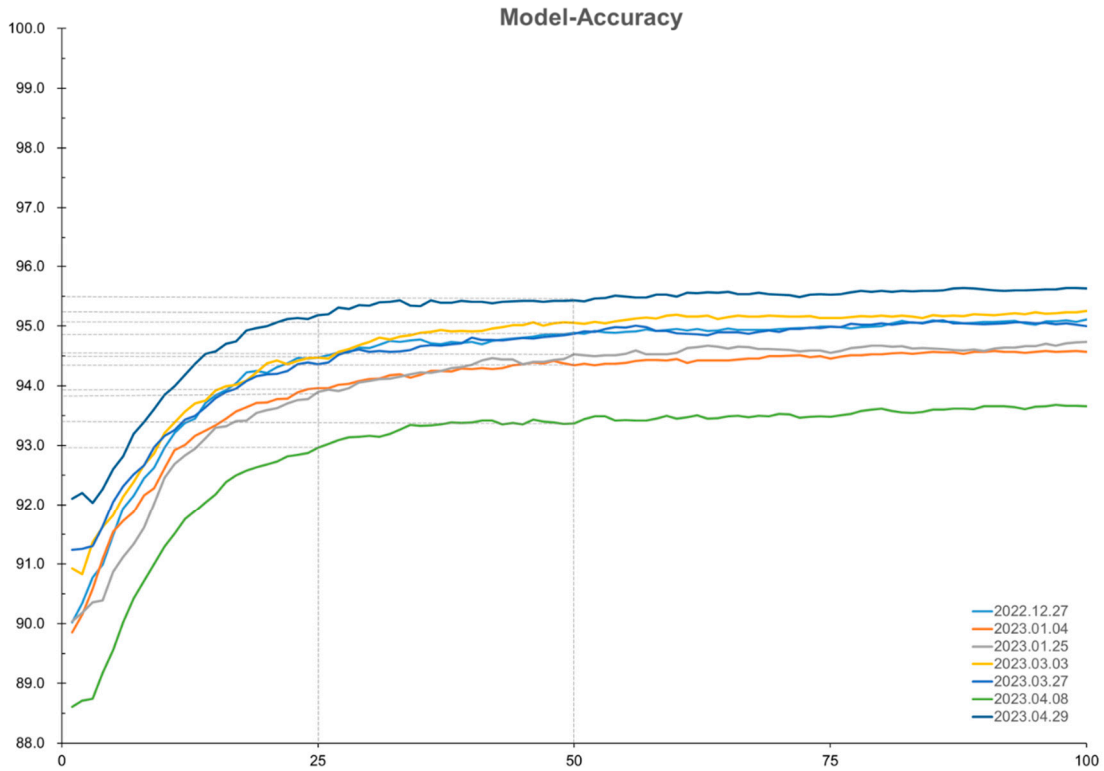

Figure 4. The accuracies of models corresponding to each image.

Preprints (www.preprints.org) | NOT PEER-REVIEWED | Posted: 9 August 2023 doi:10.20944/preprints202308.0764.v1

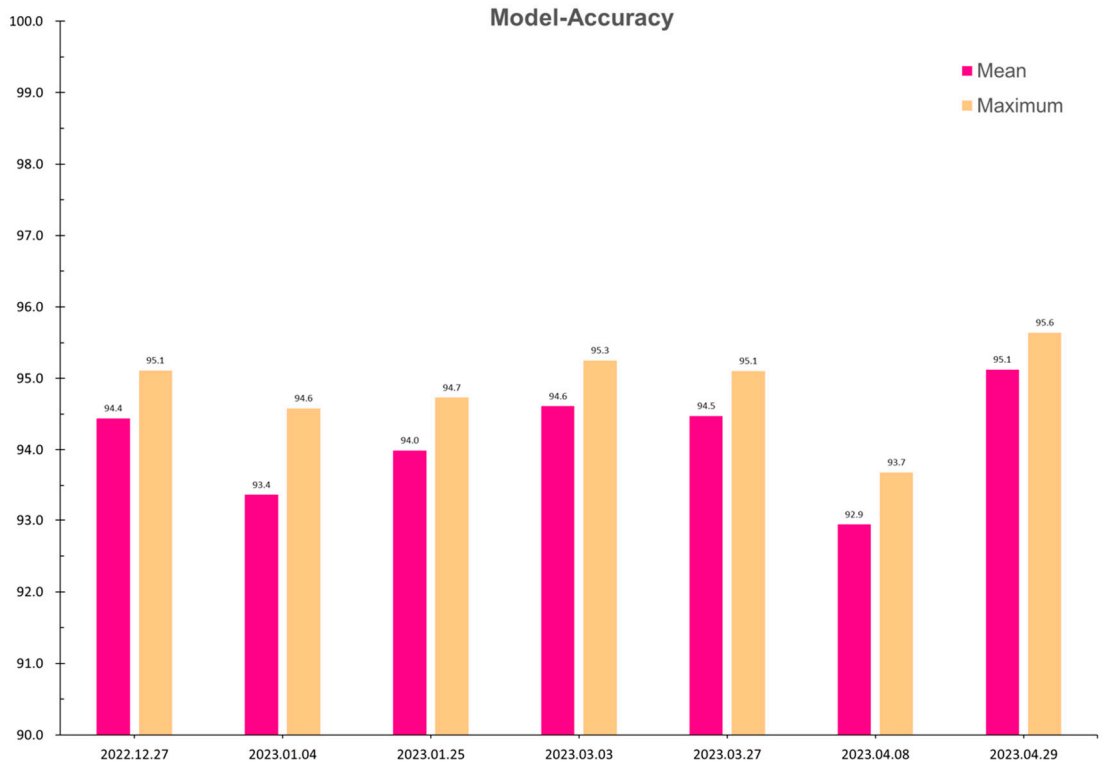

Figure 5. The accuracies of models corresponding to each image.

4.2. The Classified Images and Accuracies

GF-1 WFV has only 4 bands, namely blue, green, red, and near infrared. These bands are the basic features that may be used for the classification. However, according to our previous study [50], every two spectral bands of 4 bands were used to calculate a NDVI like index and add as the input features. Figure 6 shows the classified images for all 7 dates. The accuracies are listed in the Table 6.

According to the Table 6, in term of overall classification performance, the OA for 7 classifications was between 86.8 and 92.5, Kappa between 84.0 and 91.0, F1-Score between 82.1 and 90.1. After the visual check of all classified images and looking at all these overall performance accuracy indictors, it concluded that these classifications were well preformed. Irrigation is the focus for this study. in the training phase, two kinds of irrigation condition were identified. Irrigation 1 represented the fields with surface water or frozen ice and Irrigation 2 represented the fields without surface water but with high soil moisture. The F1-scores for irrigation 1 on Dec. 17, Jan. 4 and Jan. 25 were very high. In other 4 dates, two kinds of irrigation condition were classified and the F1- scores were not kept the same high. The F1-scores for irrigation 1 were decreased a lit and the F1-scores for irrigation 2 were in a large range of 72.7 to 95.8. These two types were still able to be separated.

Table 6. Accuracies for all date.

	2022/12/27	2023/01/04	2023/01/25	2023/03/03	2023/03/27	2023/0408	2023/0429
OA	92.5	90.3	89.8	88.8	91.1	86.8	90.9
Kappa	91.0	88.0	88.0	87.0	89.0	84.0	89.0
F1-score	90.1	85.9	84.2	83.7	86.7	82.1	86.5
I1	97.2	97.1	92.2	88.1	87.2	91.7	86.0
I2	-	-	-	72.7	75.6	80.3	95.8
WW	93.4	75.9	73.0	82.9	97.6	83.5	95.1
SC	85.7	79.3	81.4	59.1	61.6	55.4	63.3
BC	83.4	75.4	73.2	60.5	74.0	82.4	86.3

Preprints (www.preprints.org) | NOT PEER-REVIEWED | Posted: 9 August 2023 doi:10.20944/preprints202308.0764.v1

GH	91.9	87.5	81.6	96.1	96.7	81.0	87.2
OC	86.8	93.7	73.4	87.2	82.2	83.2	96.1
PT	77.1	63.0	63.7	77.5	71.7	39.2	68.2
BU	94.1	92.0	93.4	92.4	93.6	90.3	93.7
BL	89.7	91.5	95.5	86.4	95.3	59.3	86.3
DF	85.8	82.0	95.4	89.6	94.3	88.7	82.4
EF	98.1	98.3	99.2	98.4	99.4	95.1	91.9
WB	97.5	95.0	95.5	97.0	97.3	93.8	93.3

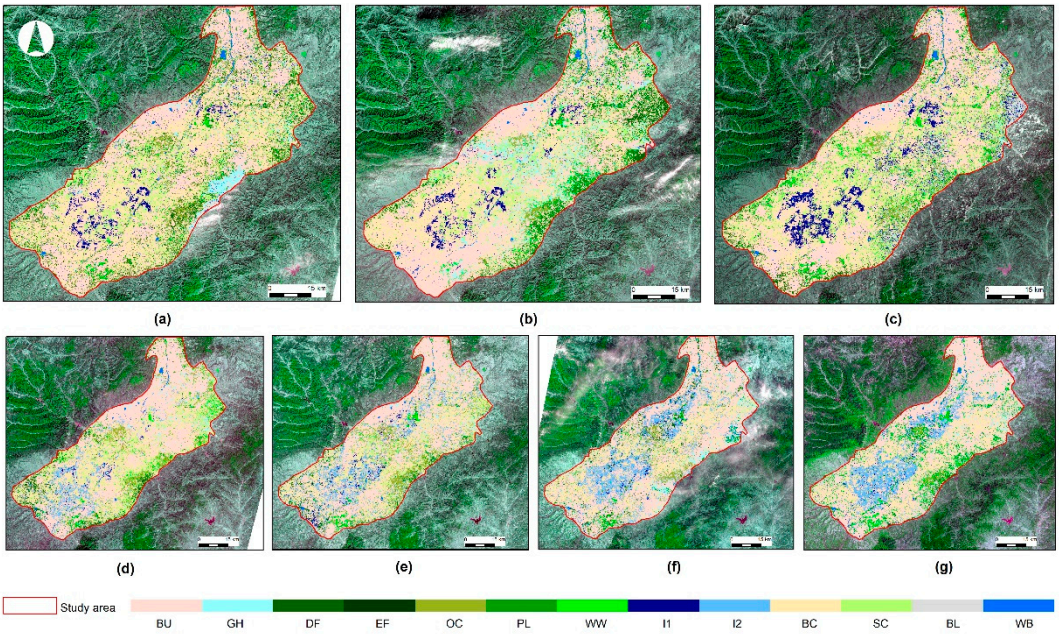

Figure 6. The classified images: (a) on Dec. 27, 2022, (b) on Jan. 4, 2023, (c) on Jan. 25, 2023, (d) on Mar. 3, 2023, (e) on Mar. 27, 2023, (f) on Apr. 8, 2023, (g) on Apr. 29, 2023, respectively.

4.3. The irrigated area analysis in watersheds

According to the time series of satellite images, it found that irrigation carries out in early November when the quite few fields were irrigated and unfortunately there was no valid GF-1 satellite image of covering entire study area available for this study. As it was in winter and the temperature went down to below zero gradually, the irrigated fields were covered by frozen ice due to the cold temperature. The irrigated fields found were increased and suspended in December and January. Ice starts to melt in later February, and the newly irrigated fields were found again in March and April as it is able to apply irrigation. The largest irrigation area is to be identified in later April as the sowing happens in May and the fields must dry up for sowing. Based on these classified images, the irrigation area on each date was calculated for each watershed. The Table 7 lists the statistics of irrigation conditions on 7 dates for 3 watersheds in the study area.

Fen River irrigation area is the largest one in the study area. The area of irrigated fields identified in frozen winter season accounted for 13.7% of total irrigatable land and the area of irrigated fields before sowing increased and accounted for 43.9%. As a tributary of Fen river, Wenyu river irrigable land ranks the second. The area of irrigated fields in winter reached to 11.0% of total irrigatable land and the area of irrigated fields before sowing increased to 35.6%. Xiao river irrigation area is the smallest one. The area of irrigated fields identified in frozen winter season accounted for 12.3% of total irrigatable land and the area of irrigated fields before sowing increased and accounted for 33.0%.

Preprints (www.preprints.org) | NOT PEER-REVIEWED | Posted: 9 August 2023 doi:10.20944/preprints202308.0764.v1

Table 7. The irrigation area for 3 watersheds (Unit: km²).

			Fen River		Wenyu River	Xiao River	
	sum	I1	I2	I1	I2	I1	I2
2022/12/27	98.6	65.8	-	22.9	-	9.9	-
2023/01/04	166.9	115.1	-	33.9	-	17.9	-
2023/01/25	208.0	143.1	-	37.6	-	27.3	-
2023/03/03	292.8	10.2	166.1	3.4	98.5	1.1	13.5
2023/03/27	538.0	6.2	306.4	1.3	166.0	0.3	57.8
2023/0408	623.1	9.4	436.2	0.7	107.2	0.3	69.3
2023/0429	653.8	5.8	453.1	1.1	120.5	0.9	72.4

5. Discussion

In this study, only 7 scenes of GF-1 images out of growing season were valid for identifying the irrigated fields. The irrigated fields were able to be visually identified but it did not answer which day irrigation was applied. Shallow surface water or soil water in a few irrigated fields evaporates over time. To distinguish this kind of dry up of irrigated field from other classes becomes indistinct due to the long interval between two satellite images. Ideally, if daily and high quality satellite images are available, it can identify the new irrigation event in time. In this sense, many more other high resolution satellite data should be integrated in the study in near future.

Irrigation 2 represents the fields with the high soil moisture but without surface water. Due to the cold temperature and less evaporation in winter, no classification samples for irrigation 2 were identified on the images of Dec. 17, Jan. 4 and Jan. 25. All irrigation samples represent irrigation 1 as the irrigated fields were frozen. In the other 4 dates, the two kinds of irrigation conditions in the field were able to be identified. In this study area, farmers conduct irrigation to the bare arable land as early as the winter comes. It is easier to identify the irrigated field from bare land than vegetated fields. So, this case study may complement the consideration of those researchers who are developing irrigation map for a large area or at a global level. There is another window out of growing season to map the irrigated fields.

However, this irrigation was a kind of cultivation management in the region in order to increase crop yield in next year. Our purpose was to know how many and in which fields irrigation has applied before the sowing in May in spring. How much water applied is another point to study but it is not able to answer in this study. Moreover, when irrigation applied is not key fucus for this study as irrigation water was poured into the bare arable land. This kind of irrigation is a flood irrigation and a large volume of water was poured into the field as such surface water was found in the fields. As the air temperature goes up in spring, the water in the fields gradually disappears. The fields have to keep appropriate soil moisture for sowing in spring. On the image of April 29, 2023, it still found water on the field surface. These fields were not able to sow in time. Therefore, the answer to the economic and minimum amount of water put into the field also needs to be further investigated.

Irrigation out of growing season has advantage to protect the ecosystem. This kind of irrigation may help reduce the wind erosion due to wet soil in the field surface when the strong wind happens in spring. But a large volume of water applied also brings some adverse ecological effect on the farming system. Sowing has to be postponed due to wet soil in the field. Soil salinization is another adverse effect induced by irrigation. Large volume of water speeds up evaporation in spring and brings the salt in deep soil back to the field surface. The other effect on the ecologic system imposed by irrigation out of season should be further investigated in near future.

6. Conclusion

This study explored the remote sensing-based classification approach to identify irrigated fields out of growing season in the winter of 2022 to 2023. 7 scenes of valid GF-1 satellite images were used to retrieve irrigated fields with a Random Forest algorithm in Jinzhong basin of Shanxi province, China. The results manifests that the method developed in this study worked well and the accuracies of model and classified images were high and acceptable. It was not overperformance during the classification as the accuracies of classified image were not higher than that from models. The irrigation field mapping with GF-1 satellite data achieved the acceptable accuracy since the lowest OA was 86.8% in comparison with the model accuracy of 92.9% and the highest OA 92.5% in comparison with the model accuracy of 94.4%. The F1-scores for irrigation 1 on Dec. 17, Jan. 4 and Jan. 25 were very high and in the range of 92.2-97.2%. In other 4 dates, the F1-scores for irrigation 1 were decreased a lit and in the range of 86.0-91.7% and the F1-scores for irrigation 2 were in a large range of 72.7 to 95.8%.

It also found that irrigation carried out in early November but the quite few fields started to be irrigated and the number of irrigated fields increased and suspended in December and January while irrigated fields were covered by frozen ice and it was not able to apply irrigation due to low temperature. The irrigation carries out again as the temperature goes up in late February. The irrigation extended over dramatically in March and April. The largest irrigation area was identified in later April as the sowing happens in May and the fields must dry up for sowing. The area of irrigated fields in the study area were increasing over time with sizes of 98.6, 166.9, 208.0, 292.8, 538.0, 623.1, 653.8 km^2 from December to April, accounting for 6.1%, 10.4%, 12.9%,18.2%, 33.4%, 38.7%, and 40.6% of the total irrigatable land in the study area, respectively.

This case study manifests that there is another window out of growing season to map the irrigated fields. This knowledge may complement the consideration of retrieving irrigation map for a large area. It also found too much water was applied in this study area and a few wet fields were not able to sow in time. The positive and adverse effect on the ecologic system imposed by irrigation out of season worth being further investigated in near future in order to support sustainable water resources management in the region.

Author Contributions: Conceptualization, J. Fan, Q Su and P. Defourny; Methodology, J. Fan, Q. Su and Z Qin; Software, J. Fan and C. Zhao; Validation, J. Lv, W. Zeng, R. Pan and Y. Song; Data processing, J. Lv, Y. Liao; Writing, Q. Su and J. Fan; Comments Z. Qin and P. Defourny.

Funding: The authors are grateful for the financial support by the National key research and development program(2017YFB0504105), ESA project (Dragon 5 58944). The authors are also grateful for the valuable comments from anonymous reviewers.

Data Availability Statement: Some or all data, models, or code that support the findings of this study are available from the corresponding author upon reasonable request.

Disclosure statement: No potential conflict of interest was reported by the authors.

References

1. Mancosu, N.; Snyder, R.L.; Kyriakakis, G.; Spano, D. Water Scarcity and Future Challenges for Food Production. Water 2015, 7, 975–992.
2. Debnath S, Adamala S, Palakuru M. An overview of Indian traditional irrigation systems for sustainable agricultural practices[J]. Int J Mod Agric, 2020, 9: 12-22.
3. Deng X P, Shan L, Zhang H, et al. Improving agricultural water use efficiency in arid and semiarid areas of China[J]. Agricultural water management, 2006, 80(1-3): 23-40.
4. Mabhaudhi T, Mpandeli S, Nhamo L, et al. Prospects for improving irrigated agriculture in southern Africa: Linking water, energy and food[J]. Water, 2018, 10(12): 1881.

5. Mpanga I K, Idowu O J. A decade of irrigation water use trends in Southwestern USA: the role of irrigation technology, best management practices, and outreach education programs[J]. Agricultural Water Management, 2021, 243: 106438.
6. Nkwasa A, Chawanda C J, Jägermeyr J, et al. Improved representation of agricultural land use and crop management for large-scale hydrological impact simulation in Africa using SWAT+[J]. Hydrology and Earth System Sciences, 2022, 26(1): 71-89.
7. Ji L, Senay G B, Friedrichs M K, et al. Characterization of water use and water balance for the croplands of Kansas using satellite, climate, and irrigation data[J]. Agricultural Water Management, 2021, 256: 107106.
8. Brauman K A, Siebert S, Foley J A. Improvements in crop water productivity increase water sustainability and food security—a global analysis[J]. Environmental Research Letters, 2013, 8(2): 024030.
9. Siebert, Stefan & Doell, Petra & Hoogeveen, Jippe & Faures, Jean Marc & Feick, Sebastian. (2005). Development and validation of the global map of irrigation areas. Hydrology and Earth System Sciences. 9. 535-547. 10.5194/hess-9-535-2005.
10. Bégué, Agnès & Arvor, Damien & Bellón, Beatriz & Betbeder, Julie & de Abelleyra, Diego & Ferraz, Rodrigo & Lebourgeois, Valentine & Lelong, Camille & Simoes, Margareth & Verón, Santiago. (2018). Remote Sensing and Cropping Practices: A Review. Remote Sensing. 10. 10.3390/rs10010099.
11. Thenkabail, Prasad & Biradar, Chandrashekhar & Noojipady, Praveen & Dheeravath, V. & Li, Yuanjie & Velpuri, Naga Manohar & Gumma, Murali & Reddy, G.P. Obi & Turral, Hugh & Cai, Xueliang. (2009). Global irrigated area map (GIAM), derived from remote sensing, for the end of the last millennium. International Journal of Remote Sensing. 30. 3679-3733. 10.1080/01431160802698919.
12. Wu, Bingfang & Tian, Fuyou & Nabil, Mohsen & Bofana, José & Lu, Yuming & Elnashar, Abdelrazek & Beyene, Awetahegn & Zhang, Miao & Zeng, Hongwei & Zhu, Weiwei. (2023). Mapping global maximum irrigation extent at 30m resolution using the irrigation performances under drought stress. Global Environmental Change. 79. 102652. 10.1016/j.gloenvcha.2023.102652.
13. Zajac, Zuzanna & Gomez, Oscar & Gelati, Emiliano & Velde, Marijn & Bassu, Simona & Ceglar, Andrej & Chukaliev, Ordan & Panarello, Lorenzo & Koeble, Renate & van den Berg, Maurits & Niemeyer, Stefan & Fumagalli, Davide. (2022). Estimation of spatial distribution of irrigated crop areas in Europe for large-scale modelling applications. Agricultural Water Management. 266. 107527. 10.1016/j.agwat.2022.107527.
14. Siddiqui, S., Cai, X. & Chandrasekharan, K. Irrigated Area Map Asia and Africa (International Water Management Institute, 2016).http://waterdata.iwmi.org/applications/irri_area/.
15. Zhang, C., Dong, J. & Ge, Q. Mapping 20 years of irrigated croplands in China using MODIS and statistics and existing irrigation products. Sci Data 9, 407 (2022). https://doi.org/10.1038/s41597-022-01522-z
16. Zhao, G. & Siebert, S. Season-wise irrigated and rainfed crop areas for India around year 2005. MyGeoHUB, doi:https://doi.org/10.13019/M2CC71 (2015).
17. Ambika, A., Wardlow, B. & Mishra, V. Remotely sensed high resolution irrigated area mapping in India for 2000 to 2015. Sci Data 3, 160118 (2016). https://doi.org/10.1038/sdata.2016.118
18. Krishnankutty Ambika, Anukesh & Wardlow, Brian & Mishra, Vimal. (2016). Remotely sensed high resolution irrigated area mapping in India for 2000 to 2015. Scientific Data. 3. 160118. 10.1038/sdata.2016.118.
19. Gumma, Murali & Thenkabail, Prasad & Hideto, Fujii & Nelson, Andy & Dheeravath, V. & Busia, Dawuni & Rala, Arnel. (2011). Mapping Irrigated Areas of Ghana Using Fusion of 30 m and 250 m Resolution Remote-Sensing Data. Remote Sensing. 3. 816-835. 10.3390/rs3040816.
20. Xie, Yanhua & Lark, Tyler. (2021). Mapping annual irrigation from Landsat imagery and environmental variables across the conterminous United States. Remote Sensing of Environment. 260. 112445. 10.1016/j.rse.2021.112445.
21. Wriedt G , Velde M , Aloe A , et al. A European irrigation map for spatially distributed agricultural modelling[J]. Agricultural Water Management, 2009, 96(5):771-789.
22. Salmon, J.Meghan & Friedl, Mark & Frolking, Steve & Wisser, Dominik & Douglas, Ellen. (2015). Global rain-fed, irrigated, and paddy croplands: A new high resolution map derived from remote sensing, crop inventories and climate data. International Journal of Applied Earth Observation and Geoinformation. 38. 10.1016/j.jag.2015.01.014.
23. Lu, Y. & Song, W. & Su, Z. & Lü, J. & Liu, Y. & Li, M.. (2020). MAPPING IRRIGATED AREAS USING RANDOM FOREST BASED ON GF-1 MULTI-SPECTRAL DATA. ISPRS - International Archives of the Photogrammetry, Remote Sensing and Spatial Information Sciences. XLIII-B2-2020. 697-702. 10.5194/isprs-archives-XLIII-B2-2020-697-2020.
24. Magidi, J.; Nhamo, L.; Mpandeli, S.; Mabhaudhi, T. Application of the Random Forest Classifier to Map Irrigated Areas Using Google Earth Engine. *Remote Sens.* 2021, *13*, 876. https://doi.org/10.3390/rs13050876
25. E. D. Chaves, M.; C. A. Picoli, M.; D. Sanches, I. Recent Applications of Landsat 8/OLI and Sentinel-2/MSI for Land Use and Land Cover Mapping: A Systematic Review. Remote Sens. 2020, 12, 3062.

26. Marvin E. Bauer, Jan E. Cipra, Paul E. Anuta, Jeanner B. Etheridge, 1979, Identification and Area Estimation of Agricultural Crops by Computer Classification of LANDSAT MSS Data, Remote Sensing of Environment, 8, 77-92.
27. Badhwar, G. B. Automatic corn-soybean classification using Landsat MSS data. II. Early season crop proportion estimation. Remote Sensing of Environment, 14, 31–37 (1984).
28. Fan X S，Xu W B and Fan J L． 2015．Mapping winter wheat growing areas in the North China Plain with FY-3 250 m resolution data． Journal of Remote Sensing，19(4) : 586 — 593［DOI: 10.11834 /jrs.20154135］
29. Claverie, M., Ju, J., Masek, J. G., Dungan, J. L., Vermote, E. F., Roger, J.-C., Skakun, S. V., & Justice, C. (2018). The Harmonized Landsat and Sentinel-2 surface reflectance data set. Remote Sensing of Environment, 219, 145-161.
30. Lunetta, R.S., Johnson, D.M., Lyon, J.G., Crotwell, J., 2004. Impacts of imagery temporal frequency on land-cover change detection monitoring. Remote Sens. Environ. 89(4), 444–454.
31. Carrão, H., Gonc¸alves, P., Caetano, M., 2008. Contribution of multispectral and mul-titemporal information from MODIS images to land cover classification. RemoteSens. Environ. 112 (3), 986–997.
32. Griffiths, P. , Nendel, C. , & Hostert, P. . (2019). Intra-annual reflectance composites from sentinel-2 and landsat for national-scale crop and land cover mapping. Remote Sensing of Environment, 220, 135–151.
33. Xiong J., Thenkabail P.S., Gumma M.K., Teluguntla P., Poehnelt J., Congalton R.G., Yadav K., Thau D., 2017, Automated cropland mapping of continental Africa using Google Earth Engine cloud computing, ISPRS Journal of Photogrammetry and Remote Sensing, 126, 225–244.
34. Pierre Defourny, Sophie Bontemps, Nicolas Bellemans, Cosmin Cara, Gérard Dedieu, Eric Guzzonato, Olivier Hagolle, Jordi Inglada, Laurentiu Nicola, Thierry Rabaute, Mickael Savinaud, Cosmin Udroiu, Silvia Valero, Agnès Bégué, Jean-François Dejoux, Abderrazak El Harti, Jamal Ezzahar, Nataliia Kussul, Kamal Labbassi, Valentine Lebourgeois, Zhang Miao, Terrence Newby, Adolph Nyamugama, Norakhan Salh, Andrii Shelestov, Vincent Simonneaux, Pierre Sibiry Traore, Souleymane S. Traore, Benjamin Koetz. (2018). Near real-time agriculture monitoring at national scale at parcel resolution: Performance assessment of the Sen2-Agri automated system in various cropping systems around the world. Remote Sensing of Environment,221, 551-568
35. Bazzi H， Baghdadi N， Fayad I , et al. Irrigation Events Detection over Intensively Irrigated Grassland Plots Using Sentinel-1 Data[J]. Remote Sensing, 2020:4058.
36. Hassan Bazzi, Nicolas Baghdadi, Ibrahim Fayad, Mehrez Zribi, Valérie Demarez, et al.. Detecting irrigation events using Sentinel-1 data. IGARSS 2021, Jul 2021, Bruxelles, Belgium. pp.6355-6358, ff10.1109/IGARSS47720.2021.9553587ff. ffhal-03342931f
37. Balenzano, A.; Satalino, G.; Lovergine, F.P.; D'Addabbo, A.; Palmisano, D.; Grassi, R.; Ozalp, O.; Mattia, F.; Nafría García, D.; Paredes Gómez, V. Sentinel-1 and Sentinel-2 Data to Detect Irrigation Events: Riaza Irrigation District (Spain) Case Study. Water 2022, 14, 3046. https://doi.org/10.3390/w14193046
38. Xavier Blaes, Laurent Vanhalle, Pierre Defourny. (2005). Efficiency of crop identification based on optical and SAR image time series. Remote Sensing of Environment, 96, 352-365
39. Wenzhi Zhao, Yang Qu, Jiage Chen, Zhanliang Yuan. (2020). Deeply synergistic optical and SAR time series for crop dynamic monitoring. Remote Sensing of Environment, 247,111952
40. Orynbaikyzy, A.; Gessner, U.; Mack, B.; Conrad, C. Crop Type Classification Using Fusion of Sentinel-1 and Sentinel-2 Data: Assessing the Impact of Feature Selection, Optical Data Availability, and Parcel Sizes on the Accuracies. Remote Sens. 2020, 12, 2779.
41. Zappa, Luca & Schlaffer, Stefan & Brocca, Luca & Vreugdenhil, Mariette & Nendel, Claas & Dorigo, Wouter. (2022). How accurately can we retrieve irrigation timing and water amounts from (satellite) soil moisture?. International Journal of Applied Earth Observation and Geoinformation. 113. 102979. 10.1016/j.jag.2022.102979.
42. Liu Chunyan, Guo Tao. The Questions and Countermeasures in Fen River Irrigation Area[J]. Shanxi Water Resources, 2017(6):2.
43. Lei Jiefeng. The Current Condition and Development Plan on the Engineering Construction in Wenyu River Irrigation Area[J]. Shanxi Water Resources, 2019(6):3.
44. Huo Xiaojue. Review on the design of the Trapezoidal Channel of attached Engineering in Xiao River Irrigation Area[J]. Shanxi Water Resources, 2014(10):10-10.
45. Zhao S H, Wang Q, Yang Y P, et al. The demonstration research of GF-1 satellite data monitoring environment application[J]. Satellite Application, 2015(3): 37-40.
46. JIANG Wei, HE Guojin, LIU Huichan, LONG Tengfei, WANG Wei, ZHENG Shouzhu, MA Xiaoxiao. Research on China's land image mosaicking and mapping technology based on GF-1 satellite WFV data[J]. REMOTE SENSING FOR LAND & RESOURCES,2017,29(4): 190-196. Doi:10.6046/gtzyyg.2017.04.29
47. Jia Liu, Limen Wang, Linbo Yang, Fei Teng, Jie Shao et al.. (2015). GF-1 satellite image atmospheric correction based on 6S model and its effect. Transactions of the Chinese Society of Agricultural Engineering, 31(19), 159-168.

48. Fan, J.; Defourny, P.; Dong, Q.; Zhang, X.; De Vroey, M.; Belleman, N.; Xu, Q.; Li, Q.; Zhang, L.; Gao, H. Sent2Agri System Based Crop Type Mapping in Yellow River Irrigation Area. J. Geod. Geoinf. Sci. 2020, 3, 110–117.
49. Fan J, Defourny P, Zhang X, Dong Q, Wang L, Qin Z, De Vroey M, Zhao C. Crop Mapping with Combined Use of European and Chinese Satellite Data. Remote Sensing. 2021; 13(22):4641. https://doi.org/10.3390/rs13224641
50. Fan J, Zhang X, Zhao C, Qin Z, De Vroey M, Defourny P. Evaluation of Crop Type Classification with Different High Resolution Satellite Data Sources. Remote Sensing. 2021; 13(5):911. https://doi.org/10.3390/rs13050911
51. Calibration Coefficients for domestic satellite data (2008-2022). Available online: https://www.cresda.com/zgzywxyyzx/zlxz/article/20230410112855288395031.html (accessed on 24 May 2023).
52. Gómez C., White J.C., Wulder M. A., 2016, Optical remotely sensed time series data for land cover classification: A review, ISPRS Journal of Photogrammetry and Remote Sensing, 116, 55-72.
53. Cristina Gómez, Joanne C. White, Michael A. Wulder.(2016). Optical remotely sensed time series data for land cover classification: A review. ISPRS Journal of Photogrammetry and Remote Sensing, 116, 55-72
54. Durgun, Y.Ö.; Gobin, A.; Van De Kerchove, R.; Tychon, B. Crop Area Mapping Using 100-m Proba-V Time Series. Remote Sens. 2016, 8, 585.
55. Charlotte Pelletiera, Silvia Valeroa, Jordi Ingladaa, Nicolas Championb, Gérard Dedieua.(2016). Assessing the robustness of Random Forests to map land cover with high resolution satellite image time series over large areas. Remote Sensing of Environment,187, 156-168
56. Breiman, L. (2001): Random Forests. In: Machine Learning Vol. 45 (2001), October, No. 1, 5–32
57. Gislason, P. O., Benediktsson, J. A., & J. R. Sveinsson (2006): Random Forests for land cover classification. In: Pattern Recognition Letters 27 (2006), No. 4, 294–300
58. Pal, M. (2003): Random Forests for Land Cover Classification. In: Proceedings of the International Geoscience And Remote Sensing Symposium, 2003, 3510–3512
59. Polikar, R. (2006): Ensemble based systems in decision making. In: IEEE Circuits and Systems Magazine 6 (2006), No. 3, 21-45